Materials & Design 225 (2023) 111545

Contents lists available at ScienceDirect

Materials & Design

journal homepage: www.elsevier.com/locate/matdes

A comparative analysis between material extrusion and other additive manufacturing techniques: Defects, microstructure and corrosion behavior in nickel alloy 625

A. Carrozza [a,b,*], S. Lorenzi [a,b], F. Carugo [a], S. Fest-Santini [a], M. Santini [a], G. Marchese [b,c], G. Barbieri [d], F. Cognini [d], M. Cabrini [a,b], T. Pastore [a,b]

[a] Department of Engineering and Applied Sciences, University of Bergamo, Dalmine, (BG), Italy
[b] National Interuniversity Consortium of Materials Science and Technology (INSTM), Firenze, Italy
[c] Department of Applied Science and Technology, Politecnico di Torino, Torino, Italy
[d] Department for Sustainability - Research Centre of Casaccia, ENEA, Rome, Italy

HIGHLIGHTS

- MEX-processed alloy 625 provides spherical micro-pores and elongated macro-defects, dependent on the scanning strategy adopted.
- MicroCT analyses allowed to reconstruct the 3D structure of the macro-defects consisting in a continuous grid of interconnected hollow channels.
- The microstructure was characterized by γ-Ni grains and Mo-, Nb-, Si-rich precipitates. X-ray diffraction evidenced the presence of M_6C-type carbides.
- Core and contour had different responses to intergranular corrosion, due to the different shape and size of the secondary phase.

GRAPHICAL ABSTRACT

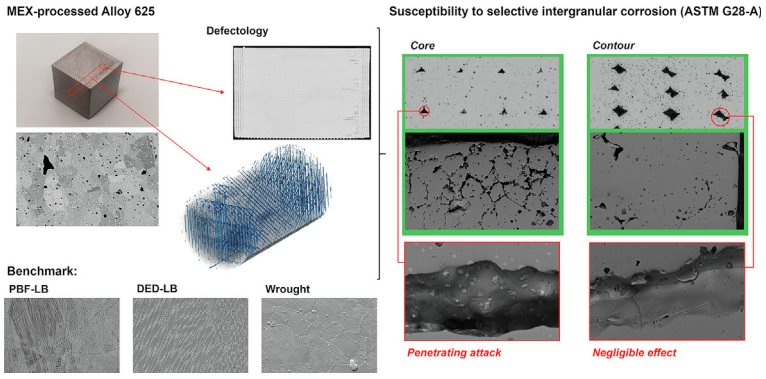

ARTICLE INFO

Article history:
Received 10 October 2022
Revised 15 December 2022
Accepted 23 December 2022
Available online 24 December 2022

Keywords:
Material extrusion
Alloy 625
Corrosion
Microstructure
Tomography

ABSTRACT

Additive manufacturing (AM) is becoming a consolidated reality for nickel alloys production in recent years. Among the several technologies available, material extrusion (MEX) is gaining industrial interest. However, its qualification is fundamental to achieve high-value applications. In this work, Ni alloy 625 produced using different AM techniques was comparatively analyzed in terms of process-related defects, microstructure and corrosion behavior. Specimens manufactured via MEX, laser powder bed fusion (PBF-LB), and directed energy deposition (DED-LB) were investigated. The MEX-produced samples showed micropores and periodically-arranged elongated macro-defects. These were analyzed in terms of image analysis and micro computed tomography. The resulting void 3D structure was mainly constituted by a grid of hollow channels, mimicking the ± 45° scanning strategy adopted. The microstructure was mainly constituted by Mo-, Nb- and Si-rich precipitates in a Ni matrix. The second phases had a blocky morphology in the core part of the material. Conversely, an elongated shape following the grain boundaries was detected in the contour. These microstructural variations impacted on the response of the alloy in an

* Corresponding author.
E-mail address: alessandro.carrozza@unibg.it (A. Carrozza).

https://doi.org/10.1016/j.matdes.2022.111545

aggressive environment (ASTM G28-A). In fact, the core underwent a localized attack, whilst the contour part was characterized by a negligible effect, as assessed in the PBF-LB and DED-LB-processed specimens.

1. Introduction

The alloy 625 (UNS N06625), also known as Inconel 625, is a Nickel-based superalloy, frequently adopted in the aerospace, chemical, oil & gas and marine industries [1]. The popularity of this material is mainly due to its excellent combination of mechanical properties, weldability, thermal stability, as well as high creep, oxidation, and corrosion resistances in host solutions [2–4]. Alloying elements - mainly constituted by Chromium, Molybdenum, and Niobium - enhance its resistance to pitting and crevice corrosion in oxidizing aqueous chloride environments, by increasing its pitting resistance equivalent number (PREN) [5,6]. Furthermore, Niobium also reduces susceptibility to intergranular attack caused by chromium and molybdenum carbide precipitation at grain the border. High strength values can be achieved via solid solution strengthening of Nb and Mo in the Ni matrix [7,8].

The alloy 625 is typically processed using conventional manufacturing technologies, such as casting or forging. However, these techniques are usually related to a low degree of material usage. In addition, the possibility to generate complex-shaped components is somehow limited. Therefore, the investigation of new manufacturing technologies to overcome these issues is industrially very relevant [9,10].

Additive manufacturing (AM) techniques fit well in this context. High material efficiencies can be achieved, as little to no machining operations are usually required. Moreover, very complex components can be built due to the layer-by-layer approach directly from a digital file, thus accelerating the project to manufacturing step [11–13]. Currently, several metal AM technologies are available in the market that can be distinguished according to several factor, such as the feedstock material form (powder, wire) or the absence/presence of a polymeric binder. Powder bed fusion – laser based, or laser powder bed fusion, (PBF-LB or LPBF) machines selectively melt prealloyed particles in a powder bed using a laser as a heat source. When the layer is completed, a new one is spread over the previous one and the process continues until the 3D component is built. This technology is very consolidated on an industrial level and grants high dimensional accuracy and the possibility to build complex parts (e.g., thin walls, hollow channels) [14–18]. Conversely, in directed energy deposition – laser based, or just directed energy deposition, (DED-LB or DED) systems, the feedstock material can be either in the form of powder or wire. In both scenarios, it is directly delivered onto the melting area and melted by a laser. The build-up rates achieved are significantly higher with respect to powder bed systems. Moreover, DED-LB can be adopted for gradient composition production and repairing/remanufacturing operations [19–21]. Material extrusion, or fused deposition modelling, or fused filament fabrication, (MEX, FDM or FFF) is a more recent commercially-available AM technology for metals, which implies the fusion of a polymeric filament filled with metal particles, generating a green part. This is subsequently debinded to remove the polymer and then sintered at high temperature, to achieve high densities. MEX-manufactured parts are usually characterized by lower dimensional accuracy and strength with respect to most of the other AM technologies [22,23]. This is generally linked to a lower density achieved in the final component. Notwithstanding that, the process time and the relative costs are greatly reduced [24]. Therefore, MEX is steadily gaining popularity in the market and commercial system from well-established firms (e.g., Markforged, Desktop Metal, BASF, Zetamix) are already commercially available [25]. Several works can be found in the literature dealing with the application of this technology in the production of different metal alloys, such as 316L stainless steel [26,27], 17-4PH [28,29], copper [30], bronze [31], Inconel 718 [32] and metal matrix composites [33].

The MEX-manufactured alloy 625 is barely mentioned in the literature [34,35] and the currently available studies do not perform an in-depth investigation of the defects, microstructure and, most importantly, corrosion behavior of the MEX-processed material. The determination of the corrosion behavior is fundamental to address, since the alloy 625 alloy is often used in very aggressive environments (e.g., both oxidizing and non-oxidizing acidic solutions, carburizing or sulfides-rich environments, chlorinated solvents) [36]. Moreover, this material is characterized by greatly differing microstructures, depending on the AM technology adopted for production. This phenomenon is mainly due to the thermal history granted by the different AM technologies being very complex and often resulting in out of equilibrium phases. Marchese et al. [37] reported the presence of Nb- and Mo-rich zones in the interdendritic areas formed upon high cooling rates, developed during solidification in the PBF-LB process. Instead, Hu et al. [38] identified Laves phases in the DED-LB-produced alloy. The presence of such microstructural features should be carefully assessed, because Laves and other intermetallic phases can significantly enhance the risk of crevice and pitting corrosion in operating conditions, as reported by Guo et al [39].

The analysis of the literature evidenced a lack of works focusing on MEX-manufactured alloy 625 with a materials-based approach. Additionally, no comparative studies with other AM technologies are available. In the end, the assessment of the corrosion behavior of the MEX-processed material is also lacking. This gap appears critical due to the typical requirements expected from this alloy, due to its typical severe application environments. Given all these literature gaps and needs, in this work a MEX-produced alloy 625 was investigated in terms of process-generated defects and microstructure. The relative effect on corrosion behavior and hardness was also assessed. The outcomes of these evaluations were then compared with the same alloy produced via other AM technologies (PBF-LB, DED-LB) and a conventional benchmark hot worked (HW) material.

2. Materials and methods

2.1. Specimens fabrication

15x15x15 mm^3 cube specimens were produced using an EOS M270 Xtended PBF-LB machine. Further information of the apparatus and the process parameters adopted can be found elsewhere [40]. The feedstock powder, supplied by EOS Gmbh, had a particle size distribution in the 16–48 μm range. Its composition is reported in Table 1. The specimens were created and uploaded in the machine using the 3D Materialise Magics software. The process parameters were selected directly from the machine interface.

2 stripes-thick 30x25 mm^2 thin wall samples were built deploying by a custom-made DED-LB apparatus, located in ENEA Casaccia research center Laboratories (Rome). The system was equipped with a 4 kW Yb fiber laser, characterized by a 1060 nm wavelength and a defocused laser spot of 1 mm diameter. A VDM Metals

Table 1
Compositions of the different feedstock materials used.

Element (wt%)	C	Si	Mn	P	S	Cr	Mo	Ni	Nb	Ti	Al	Co	Ta	Fe
PBF-LB[1]	0.01	0.08	0.03	<0.001	0.002	22.4	8.2	Bal.	3.73	0.18	<0.01	0.17	0.13	0.45
DED-LB[2]	0.01	0.07	0.01	0.003	<0.001	22.31	9.03	Bal.	3.47	0.22	0.10	0.01	0.01	0.19
MEX[3]	0.08	0.52	0.40	0.006	0.004	19.55	8.57	Bal.	3.28	0.022	<0.001	0.047	–	2.61
Wrought[4]	0.036	0.25	0.19	0.007	0.0010	21.60	8.26	Bal.	3.660	0.243	0.199	0.020	0.010	3.11
ASTM B443	Max 0.1	Max 0.5	Max 0.5	–	–	20–23	8–10	Bal.	3.15–4.15	Max 0.4	Max 0.4	Max 1	–	Max 5

[1] powder, ICP and LECO.
[2] wire, composition thermal analysis.
[3] manufactured parts, ICP and LECO.
[4] bar, ICP and LECO.

NICROFER S6020 wire with a diameter of 1.2 mm was deployed as feedstock material to perform the deposition on a stainless steel AISI 316 baseplates. The composition of the wire is reported in Table 1. The thin walls were obtained adopting a laser power of 1800 W and a 17 mm/s constant motion speed of the deposition head. The hatching distance was set to 1.5 mm. Several 15x15 mm^2 samples were extracted from the thin walls by means of mechanical cutting for microstructural analyses and corrosion tests. The sampling area was positioned in order to avoid alterations induced by atomic diffusion from stainless steel platform and wall edges (Fig. 1a). Given the simplicity of the design of these samples, no prior processing via software was needed. The samples were produced by manually controlling the movement of the deposition head via the control panel of the apparatus.

15x15x15 mm^3 cube specimens (Fig. 1b) and 15 mm-diameter 5 mm-tall cylindric specimens were built using a Metal X Markforged MEX system. The feedstock material was a commercial alloy 625 powder-filled polymer filament, supplied by the producer of the machine and characterized by a diameter of approximately 1.8 mm. Its composition is guaranteed to comply with ASTM B443 standard, as referenced in Table 1. The observation of the cross-sectioned wire did not evidence significant porosity in the metal particles. The composition of a cube was evaluated via inductively coupled plasma (ICP) and combustion infrared absorption (LECO) analyses to determine the main alloying elements and C content, respectively (Table 1). All the specimens have an external 4 stripes-thick contour on the sides. The inner part of the specimens deployed a ± 45° scanning strategy, whose orientation changed alternatively every layer. Conversely, the contour was characterized by parallel stripes maintaining the same orientation in every layer. A schematic representation of the different scanning strategies adopted is illustrated in Fig. 1b,c. No other process parameters had to be determined, due to the system automatically selecting them. After the deposition phase, chemical debinding was performed. To achieve that, the green parts was immersed in a boiling Opteon SF79 solvent, thus removing the primary binder. In order to conduct an efficient debinding step, the samples were frequently weighted, until a negligible variation was recorded after approximately 56 h. After this process, a semi-porous material with some binder residues was left. The final sintering step was conducted in a Markforged Sinter-1 furnace for 27 h, in an Ar protective gas flow. The sintering temperature(s) and gas flow are unknown, as the system is designed to work autonomously and these parameters are secreted. These specimens were created as. stl files using the Solidworks®. These files were then uploaded and processed using the online tool *eiger.io* from Markforged.

A 16 mm-diameter hot worked bar was used as a benchmark material. The material was supplied in the Grade 1 state, according to ASTM B446. The composition of the bar is reported in Table 1.

2.2. Metallographic investigation

All the AM-processed specimens that underwent microstructural analyses were sectioned along the Z direction. The MEX-produced cubes were cut perpendicular to the scan lines visible on the upper layer. Instead, the wrought bar was sectioned perpendicular to the extrusion direction in order to obtain 5 mm-tall cylindric samples. These were then cut at the center, parallel to the extrusion direction for microstructural investigation. All the specimens were then mechanically polished using silicon carbide papers with a progressively finer grid. The final polishing step was performed using a water-based lubricant and a 1 μm diamond paste. Porosity evaluations on the cross-sections were performed using the ImageJ software to analyze at least 15 micrographs per specimen. These were taken using a Keyence VHX-7100 optical microscope. Furthermore, a deeper analysis was conducted on the MEX-produced samples. In this case, 200x magnification micrographs were taken to cover the whole cross-section and stitched together. The specimens that underwent microstructural investigation were chemically etched using a Kalling No.2 reagent.

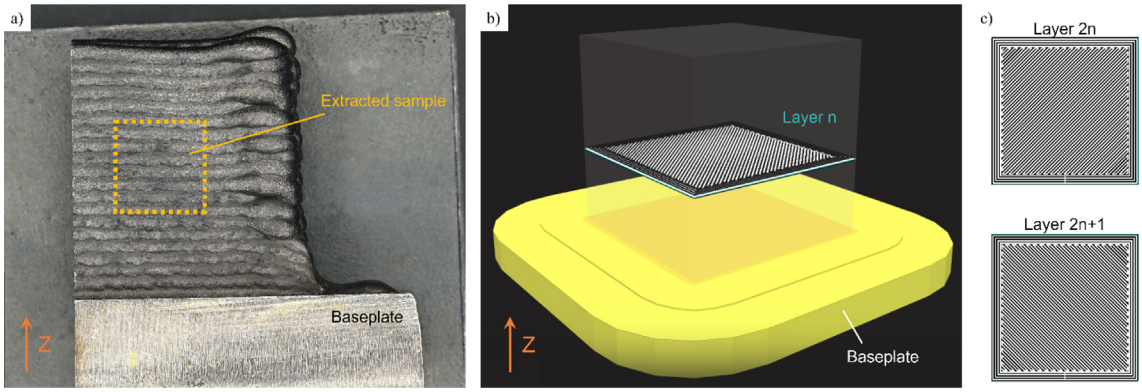

Fig. 1. A portion of a DED-LB-produced thin wall, where the area selected for the extraction of the samples is highlighted (a). Schematic representation of a MEX-built cube (b) and relative layer-by-layer comparison of the scanning strategies adopted for the contour and core portions (c).

Their observation was conducted using a Zeiss EVO 50 scanning electron microscope (SEM), equipped with an Oxford x-act probe for energy-dispersive X-ray spectroscopy (EDS).

The defects found in the MEX-produced material were further investigated by means of micro computed tomography (microCT). The samples investigated were 5 mm-tall cylinders with a diameter of 3 mm, obtained via electro discharge machining (EDM) from the central part of the material (Fig. 2), using a HB600 SSG wire cutting machine, equipped with a 0.018 mm Mo wire. By doing so, both the contour and the core portions were considered.

The tomographic unit is based on an open type X-ray source, a high-precision air-bearing rotating stage and an amorphous silicon (a-Si) sensor array detector, acquiring 16-bit grey levels with a 4096x4096 pixel matrix at 100 μm. The MEX-processed specimens were scanned at 120 kV and 15 μA (target). An integration time of 3.2 s for each radiography was selected. The X-ray beam was filtered placing a 1 mm thick sheet between the X-ray emission spot and the sample. By doing so, low-energy X-ray photons were removed from the beam's spectrum enhancing the radiography's quality. The angle step between radiographies, chosen according to the Nyquist theorem, was 0.1125°. During acquisition, the projections were corrected for charge accumulation of the detector (so called "dark-field") and were normalized by "bright-field" correction. The latter characterizes the non-uniform system response due to variation in detector sensitivity and X-ray source flux density. The normalized projections were reconstructed in VGStudioMax® based on the implemented Feldkamp filtered back projection and beam hardening correction techniques. To achieve the effective microCT resolution of about 2.98 μm, special calibration measurements were done using calibrated ruby spheres (Renishaw®, A-5000–7812: ball grade 5 according to ISO 3290, deviation of spherical form from the nominal shape of 0.13 μm). Further details can be found elsewhere [41].

The MEX-produced specimens were also investigated by means of X-ray diffraction (XRD). For assessing any possible differences between the contour and the core, these two portions were mechanically separated and investigated separately. The analysis was conducted using a Bruker Advance D8 diffractometer, deploying a 1.541 Å wavelength Cu K_α radiation. The instrument was set to work at 40 kV and 40 mA, considering a step size of 0.01°. The Ni cubic cell parameter (a_o) was evaluated by combining the cubic systems governing equation and Bragg's Law [42]. Further details on the methodology can be found elsewhere [43].

Vickers hardness was assessed by means of a UHL VMHT microhardness tester, set to apply a load of 1000 gf for 15 s. A minimum of 15 indentations per sample were performed.

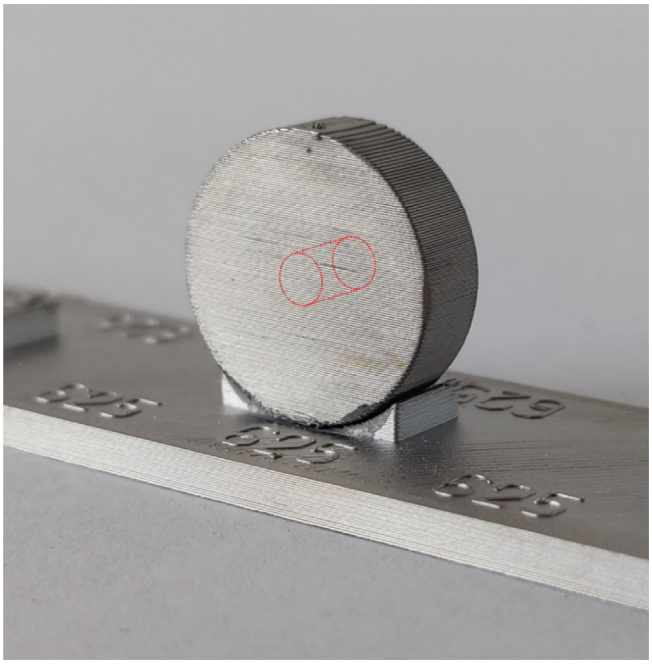

Fig. 2. MEX-produced cylindrical samples. The highlighted area represents the portion that was extracted by means of EDM cutting for microCT analyses.

2.3. Corrosion testing

Wrought, PBF-LB-, DED-LB- and MEX-produced specimens were tested for susceptibility to selective intergranular corrosion in a boiling ferric sulfate/sulfuric acid environment for 120 h, in compliance with ASTM G28-A. Prior to testing, the specimens were mechanically ground by SiC papers. The aim of this operation was to achieve a surface finishing that allowed to ignore possible differences generated by the different manufacturing technologies adopted. Before the immersion, the specimens were rinsed with water, cleaned in an acetone ultrasonic bath, dried and weighed, using an analytic balance. These operations were also performed after exposure for evaluating the mass loss and corrosion rate. The corrosion morphology was investigated by means of SEM observations of the cross-sections.

3. Results and discussion

3.1. Defects analyses

The average porosity evaluated by means of image analyses is reported in Table 2. The PBF-LB- and DED-LB-processed specimens were characterized by significantly low values. These results tie well with findings in the recent literature [44–46] and confirm that PBF-LB and DED-LB technologies are currently well established and the relative process parameters are optimized. Conversely, the specimens produced by MEX process were characterized by significantly higher porosity values.

It is well known that an excessive concentration of pores can result in a degradation of the corrosion behavior and mechanical properties [12,47]. It was reported that pores exceeding a 50 μm dimension might be detrimental for the corrosion behavior of AM-processed metals [12]. Therefore, the fraction of pores characterized by a Feret diameter (d_{Feret}) of 50 μm or higher was estimated. No defects above this threshold were found in the PBF-LB-fabricated specimens. Instead, in the DED-LB- and MEX-manufactured materials a relevant fraction of pores > 50 μm were found, accounting for a total of 33 % and 12 % of the total porosity, respectively.

The higher overall porosity found in the MEX-processed material was worthy of a deeper evaluation. The observation of the cross-section of a cubic sample (Fig. 3) evidenced the presence of two main types of voids:

- **Micro-pores**, randomly distributed throughout the whole cross-section of the sample.
- **Elongated macro-defects**, having a triangular (core)/quadrilateral (contour) cross-section shape, periodically distributed in a grid-like fashion.

Table 2
Porosity and relative fraction of pores > 50 μm.

Manufacturing technology	PBF-LB	DED	MEX[1]
Porosity (%)	0.06	0.06	3.04
Pores > 50 μm (%)	0	0.02	0.37

[1] Considering the whole sample, including contour.

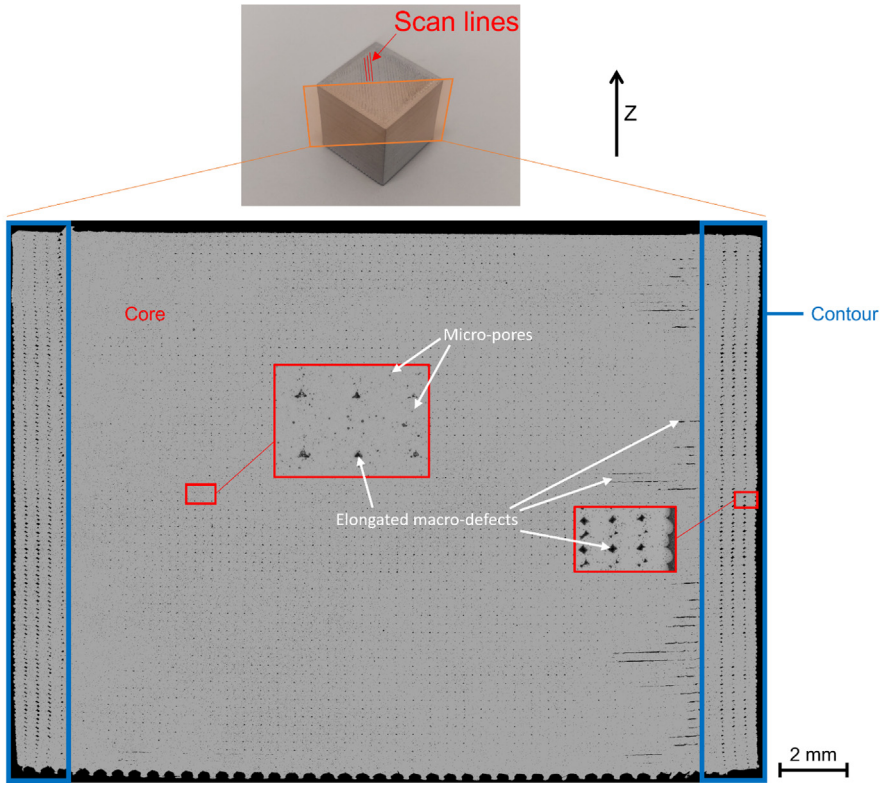

Fig. 3. Metallographic cross-section (45° cut) of a MEX-produced sample with different types of defects highlighted.

The micro-pores were the smallest defects found in the cross-section analysis. Their presence might be attributed to pre-existing gas porosities in the feedstock powder and/or the sintering step. The macro-defects were characterized by a periodical arrangement both along the Z axis and horizontally, along deposition plane. Considering a cross-section perpendicular to the deposition lines (Fig. 3), the average distance between two horizontal neighbor macro-defects was quite constant and close to 250 μm. This value corresponds to the width of a stripe post-sintering. Therefore, it is reasonable to assume that the macro-defects were created in correspondence of the area where two stripes met during the deposition phase. This remark is further corroborated by the shape of this defects. This was an upward facing triangle in the core, possibly resulting by the conjunction of a scan parallel to the metallographic section, and two perpendicular scans of the upper scan layer (Fig. 4a,b). In fact, the scanning strategy adopted implemented a 90° rotation between successive layers. Conversely, the macro-defects found in the contour were characterized by a quadrilateral shape, due to the different scanning strategy adopted in this area. In fact, no rotation was set to occur when moving to a successive layer, as visible in Fig. 4c. It is also worth mentioning that these voids appeared more elongated. A possible explanation lies is the cross-sectioning direction, which was perpendicular to the scanning lines in the core, but 45°-oriented with respect to the ones in the contour.

Micro-pores and interlayer voids were also assessed in other works [34,35]. Thomas and Gleadall [35] described interlayer defects as intentional. In fact, according to these authors, these voids should coalesce and disappear during sintering. However, these were still clearly visible in the fracture surfaces of the post-sintered specimens showed in their work. Costa et al. [34] attributed these defects with the under extrusion of the filament during deposition, or a sub-optimal optimization of the parameters.

To sum up, micro-pores can be considered intrinsic defects, caused by the quality of the feedstock material and debinding phase. Conversely, the macro-pores can be categorized as extrinsic defects, generated by the scanning strategy adopted.

The cross-sectional pore size was estimated by evaluating the equivalent diameter (D_{EQ}), using the following equation:

$$D_{EQ} = 2\sqrt{\frac{A}{\pi}} \tag{1}$$

where A is the area occupied by a given pore, obtained via image analysis. The adoption of this shape descriptor can lead to slight underestimations of the surface of the pores. Nevertheless, D_{EQ} can be a useful parameter to compare the defects in different specimens, as illustrated by other authors in the literature [48,49]. The resulting analysis, provided in Fig. 5a, describes a bimodal size distribution of the defects, characterized by a primary peak at 5 μm (peak I) (micro-pores) and a secondary peak at 30 μm (peak II) (macro-defects). The threshold between micro- and macro-defects was determined by carefully comparing a relevant ($\simeq$ 50) number of pores randomly selected in each class of the distribution. This value was found at 20 μm, which corresponds to the local minimum of the distribution. Given the limit of the DEQ as a sole descriptor of the pores shape, the pore aspect ratio (AR) was evaluated as well, using the following equation:

$$AR = \frac{d_{Feret}}{d_{Feret,min}} \tag{2}$$

where $d_{Feret,min}$ represents the minimum Feret's diameter. The vast majority of the defects in the material were characterized by an AR > 0.5, as provided in Fig. 5b. These pores can be considered quasi-spherical and are characterized by a comparatively smaller size. Lower AR values are achieved by defects progressively bigger (e.g., elongated).

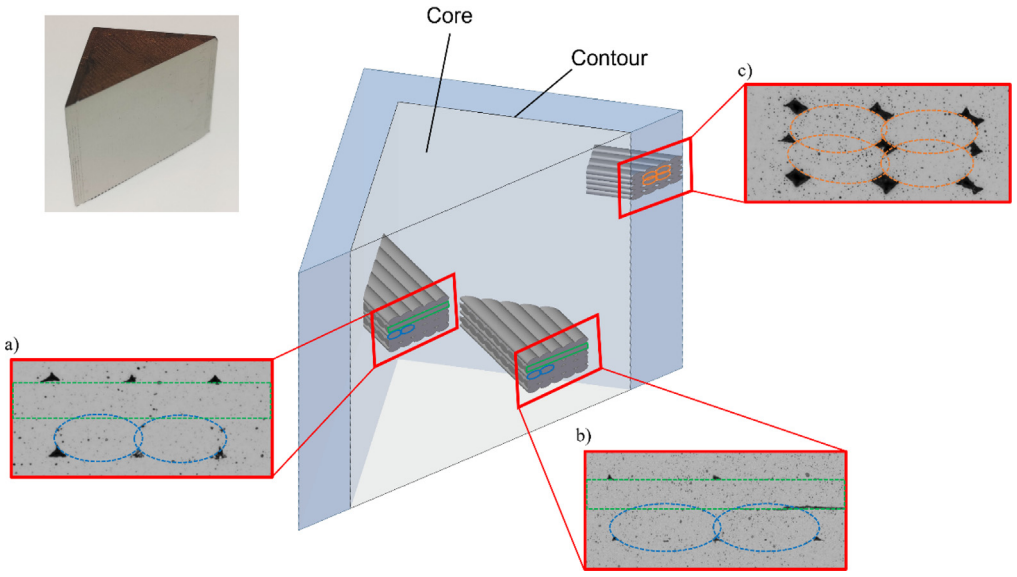

Fig. 4. Representative view of the wire scan directions and their correspondence with the locations of the triangular macro-defects in the core (a,b) and quadrilateral macro-defects in the contour (c). The green, blue and orange dashed lines represent respectively the parallel, perpendicular and 45°-oriented wire scan lines, with respect to the cross-section plane. The sizes represented were altered on purpose to improve the readability. (For interpretation of the references to colour in this figure legend, the reader is referred to the web version of this article.)

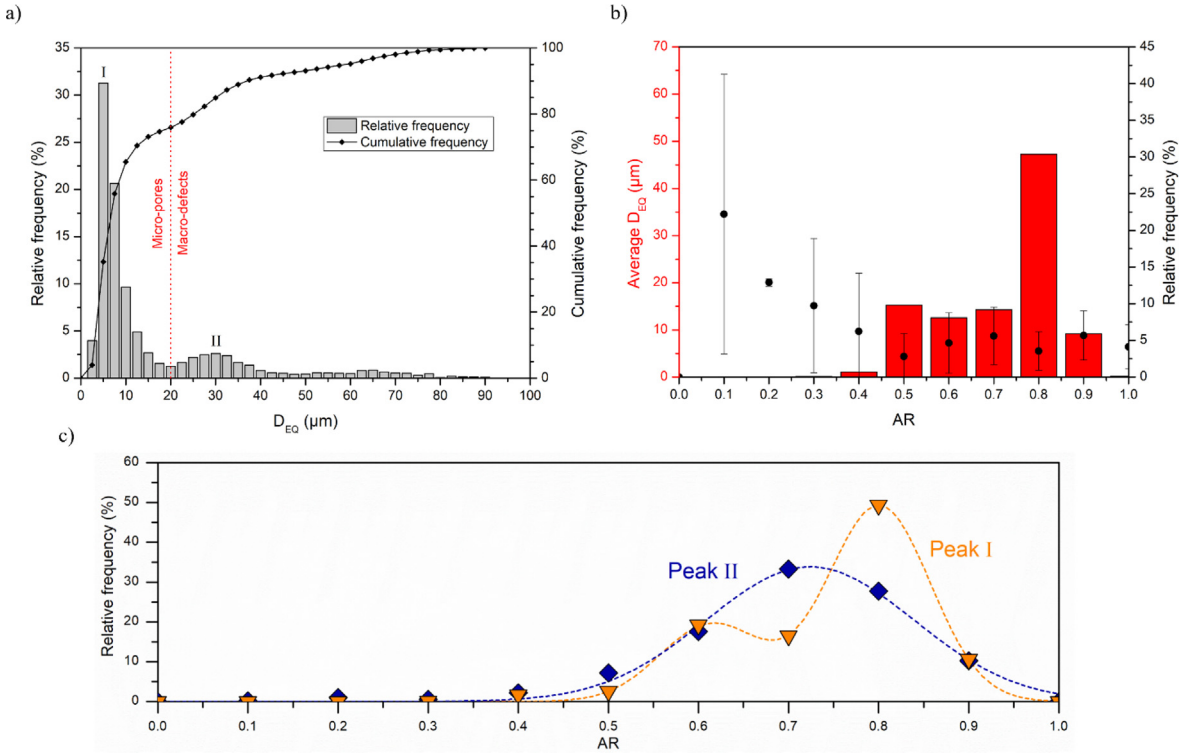

Fig. 5. Pore size distribution (a) and pore aspect ratio distribution and correlation with size (b) by image analysis of the optical micrographs of the MEX-processed samples. AR distribution of the defects falling in the peak I (3.75–6.25 μm) and peak II (28.75–31.25 μm) ranges (c).

The AR distributions relative to the main and secondary peak of the D_{EQ} distribution were also assessed to compare the pore shapes of the micro- and macro-defects (Fig. 5c). It is evident that peak I (3.75–6.25 μm) was characterized by AR distribution significantly shifted towards high values, where ≃ 50 % of the micro-pores accounted for an AR of 0.8. Conversely, a wider distribution and the shift of the main peak towards lower values was assessed for the macro-defects falling in the peak II range (28.75–31.25 μm). This analysis confirms the lower sphericity of the macro-defects with respect to the micro-pores.

The image analyses performed on the cross-section of the MEX-processed specimens highlighted the presence of a relevant number of directional macro-defects, whose cross-section analyses might be misleading due to possible underestimations of their overall volume, as these voids might achieve lengths comparable to the size of the specimen itself. This effect was suggested by

the presence of sparse elongated defects in the cross-section (Fig. 3a,4b).

A microCT analysis was conducted on a MEX-processed specimen in order to investigated the 3D void texture, assessed by means of image analysis of the cross-section. One can argue that microCT analyses are intrinsically limited by their inability to detect the smallest pores. However, du Plessis et al. [50] reported that only larger pores/defects are very important in determining the properties of an AM-processed material. Therefore, these types of analyses are very important, especially when adopted to determine the spatial distribution of the defects.

During the microCT data elaboration phase, the segmentation of the scan was performed as a two-step process. Firstly, the Otsu method [51] was applied to obtain from the original image (Fig. 6a,d) a binary image (Fig. 6b) of the sample and surrounding air. Then, the binary image was used to subtract the background (B) from the unprocessed image (I), to obtain the filtered image (I_F) (Fig. 6c), an image where the surrounding air is null, as described in the following equation:

$$I_F = I \cdot (1 - B) \tag{3}$$

The above operation was carried out as an element-wise matrix operation on each 2D projection in the 3D volume stack, thus leading to a clear bimodal voxel intensity histogram of the 3D filtered volume stack showing the void's peak and the material's peak. The midpoint between adjacent peaks was used as threshold, allowing the distinction in voids and solid material. The rendered void space in visible Fig. 7a,b. A 3D grid-like structure is evident in the core of the material (Fig. 7c). Moreover, the presence of continuous linear defects in the contour was also confirmed (Fig. 7d).

A further analysis of the defect 3D structure (Fig. 8a) evidenced the presence of significant voids in correspondence of the conjunction of the core and contour voids (Fig. 8c). The presence of such defects suggests a certain degree of connectivity between these two regions. A substantial interconnectedness was also evident in the elongated macro-defects in the core portion of the material (Fig. 8b).

The 3D void structure was sliced>2000 times along the length of the sample in order to obtain a relevant number of cross-sections (Fig. 9a). The voids found were investigated in terms of DEQ and compared with the outcome on the analysis performed via optical imaging. The result of this comparative evaluation is reported in Fig. 9b. The maximum D_{EQ} detected was significantly higher in the microCT reconstruction, reaching up to 300 μm. The microCT analysis was not able to detect most of the micro-pores, visible via optical imaging. Nevertheless, a main peak ($\simeq$ 25 μm) relative to the macro-defects was found. This value was very close to the one found using the microscope ($\simeq$ 30 μm) (Fig. 5a). Then, the outcome of both analyses seems to be in good agreement.

Therefore, the microCT analysis proved to be a very reliable technique to investigate the overall 3D structure of the voids in material and evaluate the possible interconnectedness of the pores. However, due to a lower limit in the resolution of the instrument, the detection of the smaller process-related pores was impossible. This factor is non-negligible due to the micro-pores accounting for most of the total porosity in the material (Table 2). Nevertheless, the information gathered can be used to re-evaluate the numerical values obtained in the previous analysis, based on the result gathered via optical imaging, that might underestimate the total porosity. Therefore, considering the insight on the macro-pores shape and arrangement granted by the microCT analysis, the following equation can be adopted to estimate the overall porosity of the specimen:

$$P_{tot}(\%) = 100 \cdot \frac{A_{tot}}{A_{sample}} = 100 \cdot \frac{A_{tot}^{micro} + A_{contour}^{macro} + 2 \cdot A_{core}^{macro} - A_{core}^{elongated}}{A_{sample}} \tag{4}$$

where P represents the porosity and A the area measured via image analysis. The threshold between micro- and macro-pores was considered 20 μm, as discussed before. The terms micro and macro refer to the micro- and macro-porosities, respectively. Instead, the terms tot, contour and core refer to the whole volume of the samples, its contour and core portions, respectively. The term $A_{core}^{elongated}$ represents the area relative to the elongated macro-pores parallel to the cross-section direction (for reference, see Fig. 3). The re-evaluation of the total porosity according to Eq. (4) provided a value of 3.54 ± 0.07 %, thus an increase of approximately 16 %.

3.2. Investigation of the microstructure

The optical micrographs obtained from the PBF-LB-processed samples (Fig. 10a) highlighted the presence of columnar grains, grown epitaxially along the building direction Z, and visible melt pools, in agreement with the literature [52]. Instead, the DED-LB-processed material was characterized by large dendritic regions (Fig. 10b), as confirmed by other works [53,54]. Conversely, the MEX-processed samples (Fig. 10c) had a precipitates-rich microstructure in a Ni matrix. Moreover, some inclusions were seldom detected inside some pores and accounted for 0.33 % of the total cross-section area. The benchmark HW material (Fig. 10d) was characterized by equiaxed Ni grains with characteristic twins, a typical outcome for the annealed alloy 625 [55].

A further microstructural characterization was conducted via SEM imaging (Fig. 11). The PBF-LB-processed samples (Fig. 11a) provided a dendritic/cellular microstructure. Nb and Mo segregations were detected in correspondence of the interdendritic regions, in agreement with other works in the literature [56,57]. Moreover, no precipitates were found. However, Marchese et al. [58] demonstrated via transmission electron microscopy analysis (TEM) that very small (<100 nm) Nb-rich MC carbides are present in the PBF-LB-manufactured material. Conversely, Mo-rich precipitates were detected in the interdendritic regions of the DED-LB-processed specimens (Fig. 11b), as confirmed by Abioye et al. [59]. These were identified as Laves phases by Yangfan et al. [60] and Hu et al. [61]. Moreover, some small ($\simeq$ 1 μm) oxide inclusions

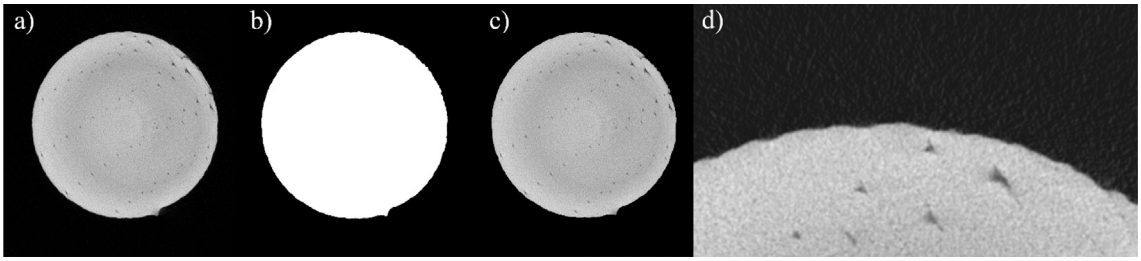

Fig. 6. Unprocessed image slice I (a), binary image B (b), filtered image slice I_F (c) and detail of I (d).

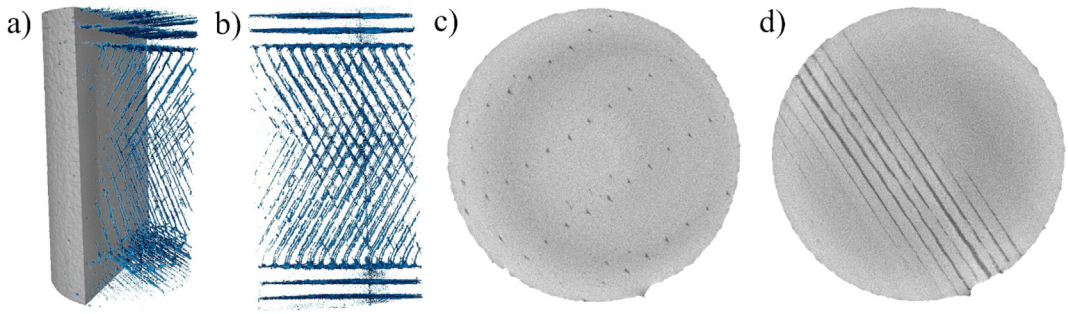

Fig. 7. MicroCT render of a MEX-processed sample (a) and the relative void space (b). Representative slice of the core region (c) and contour (d). The void space is underlined and colored in blue in the render. (For interpretation of the references to colour in this figure legend, the reader is referred to the web version of this article.)

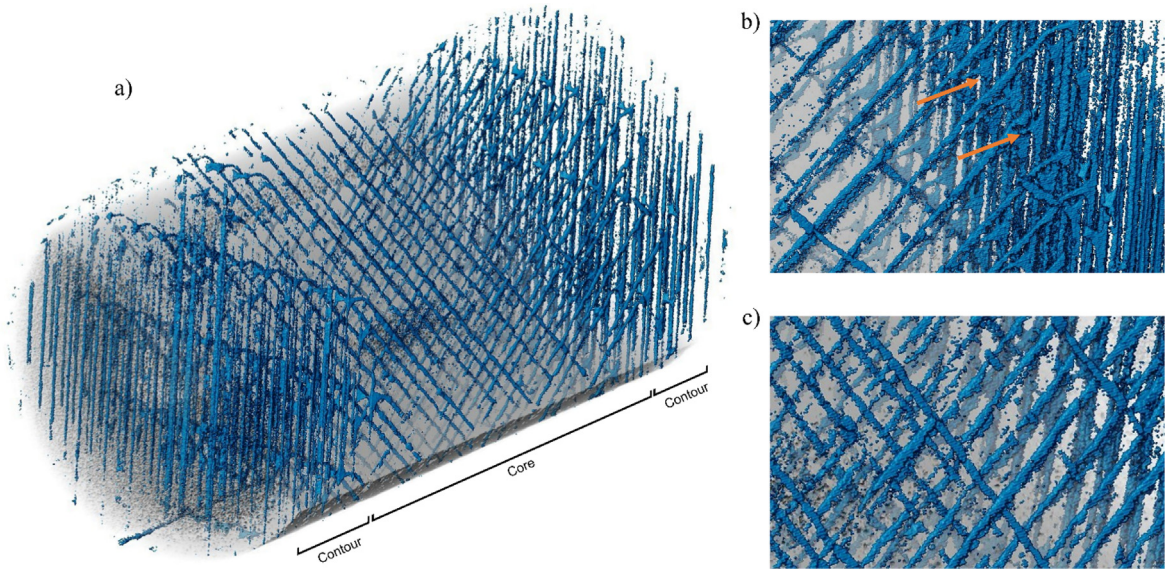

Fig. 8. 3D void structure (a) with relative core-contour interface voids (orange arrow) (b) and macro-defects 3D grid-like structure highlighted (c). (For interpretation of the references to colour in this figure legend, the reader is referred to the web version of this article.)

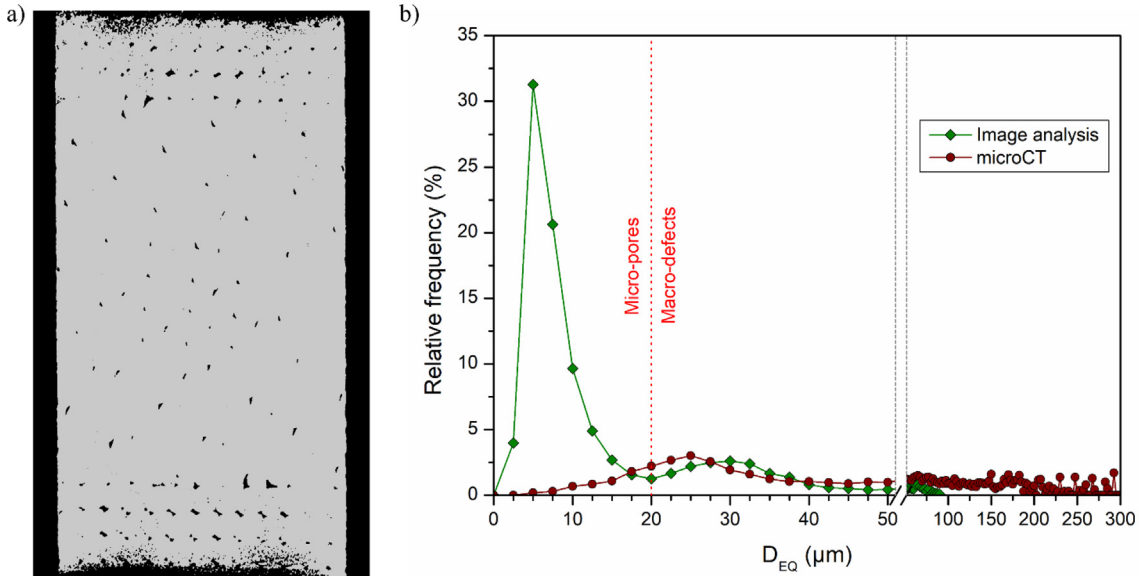

Fig. 9. Representative slice of the microCT used for pore analysis (a). D_{EQ} relative distributions comparing the outcome of the optical microscope and microCT analyses (b).

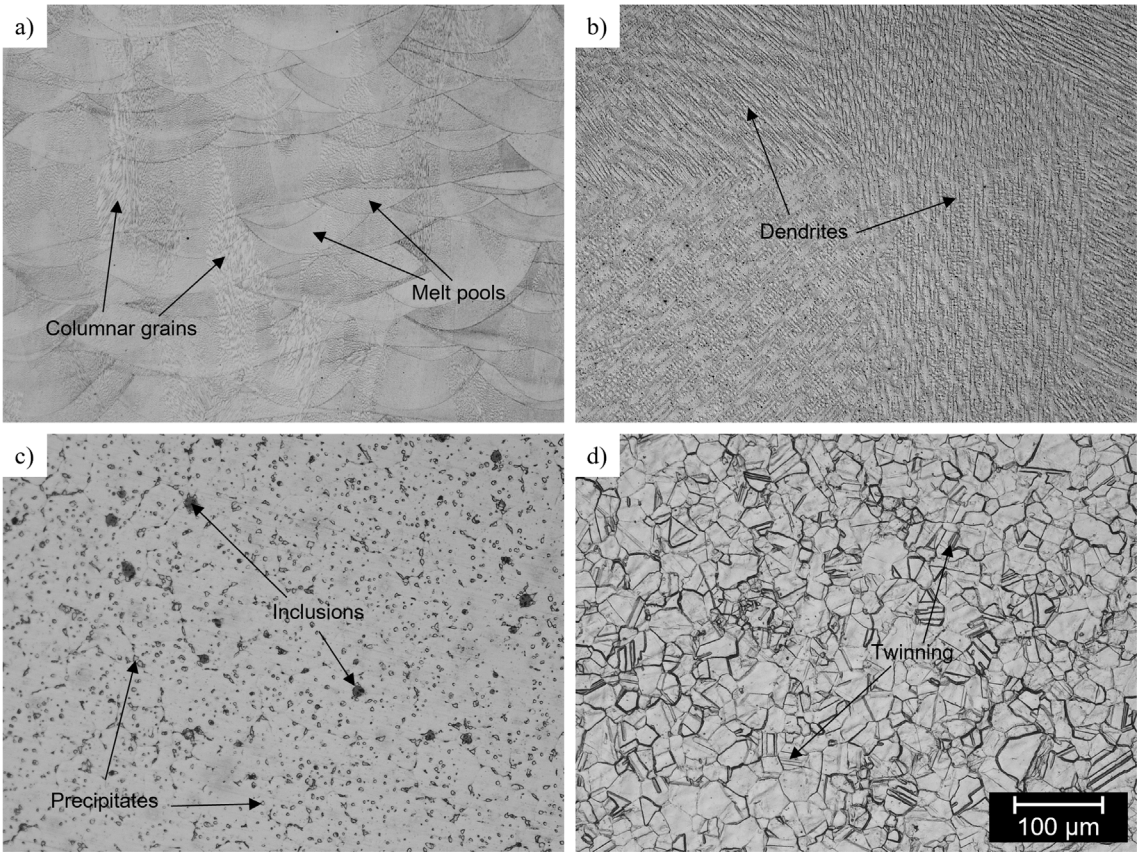

Fig. 10. Optical micrographs of the PBF-LB- (a), DED-LB- (b), MEX-processed (c) and HW (d) specimens.

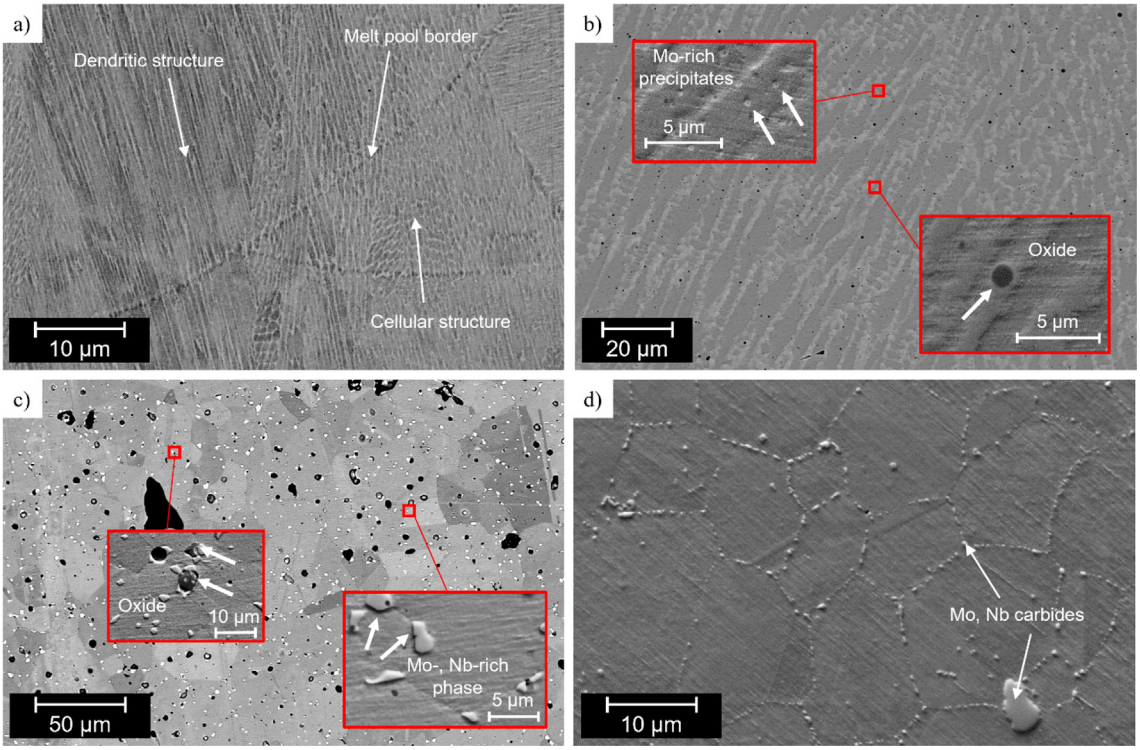

Fig. 11. SEM micrographs of the PBF-LB- (a), DED-LB- (b), MEX-processed (c) and HW (d) specimens.

were also found. Similarly, spherical oxides rich in Ti, Al and Cr were also detected by Huebner et al. [62]. These were probably generated during the manufacturing operations due to the high affinity of these elements with oxygen and the lack of a sealed process chamber. In the MEX-processed specimens, similar oxide inclusions (Fig. 11c) were also detected. These were found to be rich in Al, Si and Cr by EDS analyses (Fig. 12). It is worth noticing that these oxides were surrounded by secondary phase. The formation of oxidized areas, alongside carbides, is expected to form during the debinding/sintering phases as a result of impurities pick-up [63]. Working on the MEX-processed Inconel 718 alloy, similar considerations were also made by Thompson et al. [32]. Carbides were found throughout the whole microstructure of the MEX-processed material in a blocky shape both inside and at the border of grain boundaries. SEM observations also evidenced the presence of a second phase (Fig. 11c), evenly dispersed in the material (approximately 3.2 % in volume). It was abundantly found in correspondence of grain boundaries and pore/inclusion edges, more seldom inside the grains. This secondary phase was rich in Mo, Nb and Si (Fig. 13a). By comparing its EDS spectrum with the one relative to the matrix (Fig. 13b), a slight enrichment in C was also detected in this second phase. Moreover, it appeared depleted in Ni, Cr and Fe with respect to the matrix. The benchmark HW material was characterized by elongated carbides, forming semi-continuous chains along the γ grain boundaries, in agreement with the literature [64]. The second phase was constituted of MC-type carbides, rich in Mo and Nb, whose elongated shape is due to the low cooling rate achieved at the end of the hot working process [65].

Since the phase investigation of the MEX-processed alloy 625 is a current literature gap, a XRD analysis was conducted (Fig. 14). Apart from the Ni(γ) matrix, the peaks relative to M_6C-type carbides were detected [66–68]. To confirm this assumption, the cell parameter (a_0) was estimated. This equaled 11.06 ± 0.01 Å, which fits well with other values found in the literature for the alloy 625, ranging from 11.09 to 11.2 Å [69,70]. Furthermore, the EDS average composition, relative to the main alloying elements, in the precipitates was found to be comparable with similar evaluations found in the literature for M_6C carbides in alloy 625, as summarized in Table 3.

3.3. Hardness

The average Vickers microhardness was evaluated for all the AM-processed specimens, providing the values reported in Fig. 15. The specimens manufactured via PBF-LB resulted in the highest hardness values, mainly due to the very small size on the dendritic regions (Fig. 11a). These were slightly larger in the DED-LB-produced specimens, leading to a decrease in terms of hardness. Finally, these structures were completely absent in the MEX-processed material, characterized by far by the lowest hardness (189 ± 11 HV).

3.4. Corrosion behavior

Susceptibility to intergranular corrosion tests were conducted to evaluate the corrosion rates of the alloy 625 processed using different AM technologies. The results, presented in Table 4, were also compared with the HW benchmark material.

The DED-LB-processed material provided an excellent corrosion rate (<100 mdd), whilst the MEX-manufactured specimens provided the highest v_{corr} among all the AM technologies considered

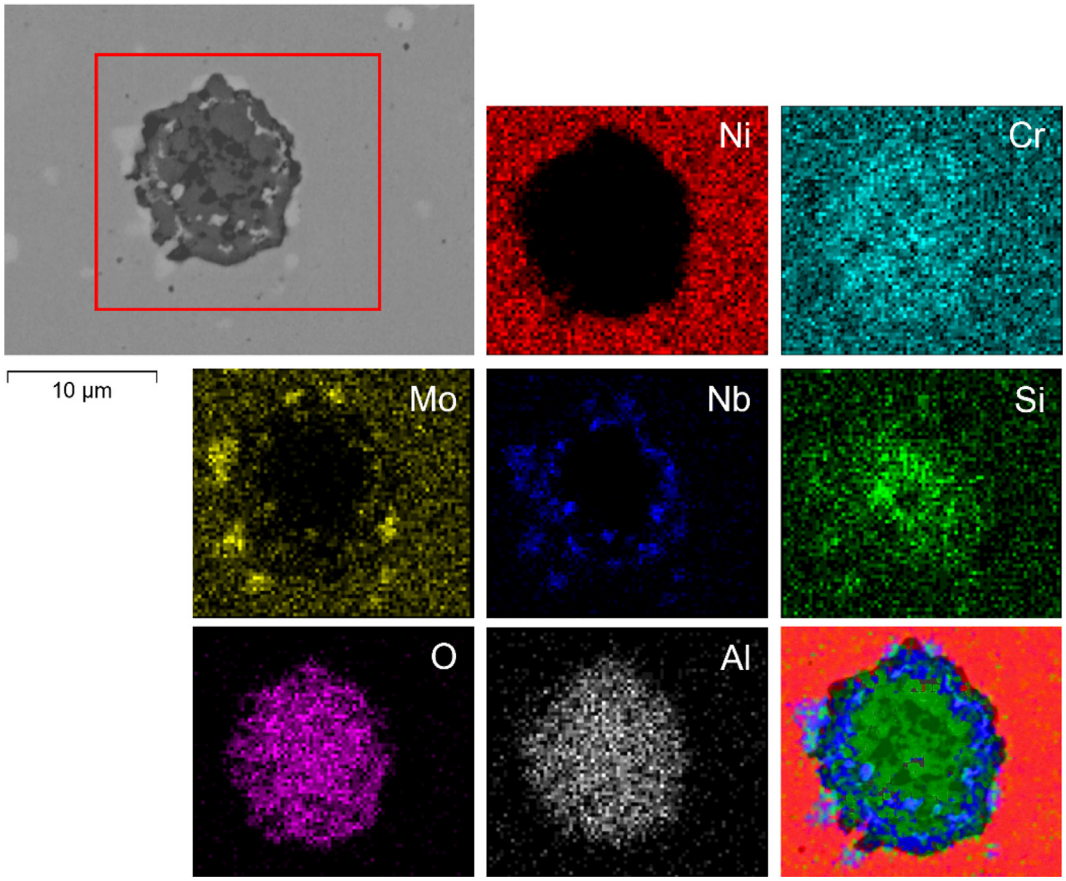

Fig. 12. EDS map analysis covering an oxide inclusion found in the MEX-processed alloy 625.

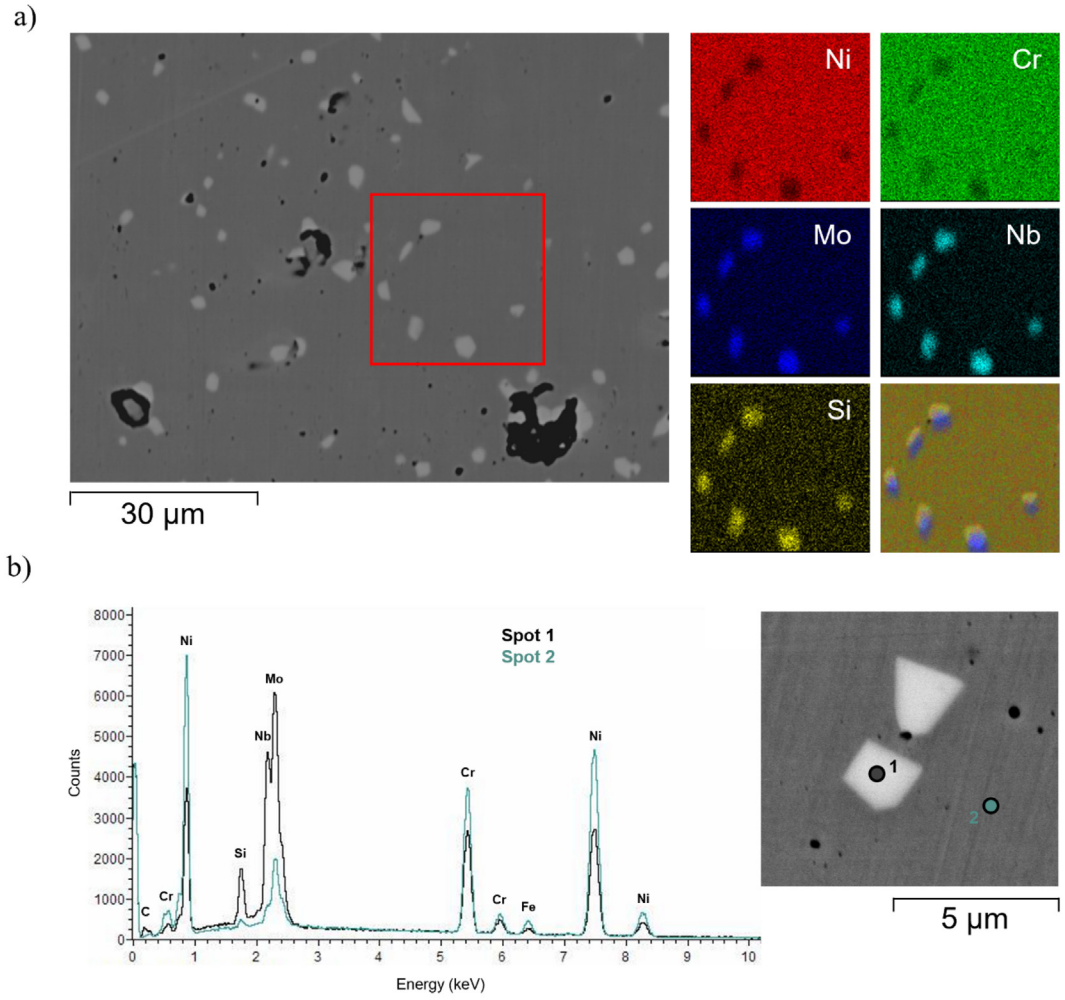

Fig. 13. EDS map performed on the MEX-processed alloy 625 (a) and relative comparison of the diffraction pattern of the secondary phases found and the matrix (b).

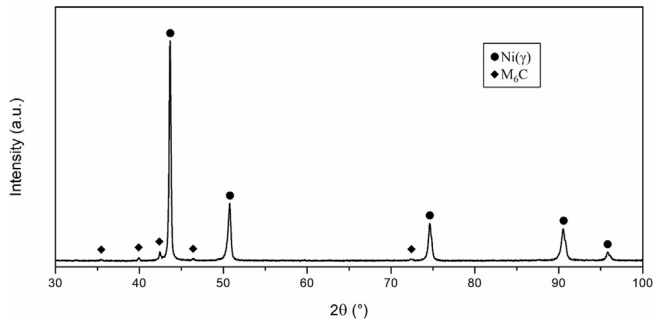

Fig. 14. XRD pattern of the MEX-processed alloy 625.

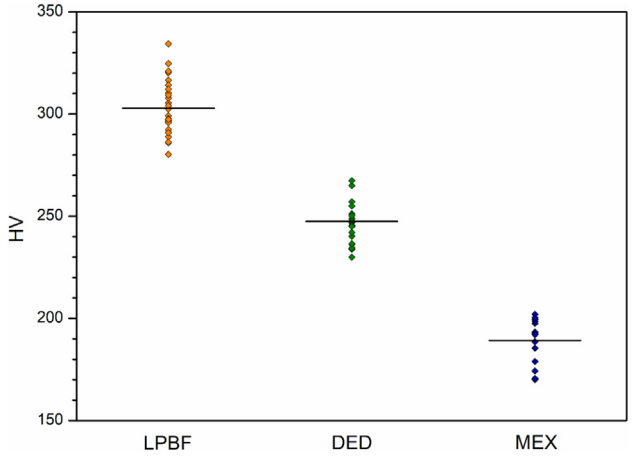

Fig. 15. Outcome of the Vickers microhardness test for the AM-processed specimens (the horizontal lines represent the average values).

in this work. Notwithstanding that, this value was significantly lower than the HW benchmark material. The significantly higher corrosion rate of this latter condition was mainly due to grain

Table 3
EDS composition of the Mo- and Nb-rich phase and comparison with M_6C carbides composition in the alloy 625 from the literature.

Source	Ni (at.%)	Cr (at.%)	Nb (at.%)	Mo (at.%)	Si (at.%)
This work	33.3 ± 2.6	19.4 ± 0.4	19.7 ± 2.0	19.4 ± 0.9	8.1 ± 0.3
Ferrer et al. [71]	26.0	15.0	13.5	40.0	5.5
Cieslak et al. [72]	39.0	20.3	24.2	14.1	2.3

Table 4
Corrosion rates evaluated according to ASTM G28-A. The data relative to the PBF-LB-produced and HW samples come from a previous publication [73].

Specimen	Exposed surface (cm^2)	Mass loss (g)	v_{corr} (mdd)	Source
PBF-LB	13.4	0.11	167	[73]
DED-LB[1]	11.7	0.04	75	–
MEX[2]	15.2	0.16	214	–
HW	6.1	0.11	345	[73]

[1] 15x15 mm^2 specimens extracted from the thin walls.
[2] 15x15x15 mm^3 cube.

dropping phenomena occurring during the test, as already discussed in a previous work [73].

No significant proofs of an intergranular attack were found in the PBF-LB- and DED-LB-processed material (Fig. 16a). Conversely, the MEX-manufactured specimens provided a dissimilar behavior during the test, according to the area of the sample considered. This phenomenon is illustrated in Fig. 16b,c. The core portion of the material highlighted a penetrating attack, following the grain boundaries and macro-defects, extending for>200 μm (Fig. 16b). Oppositely, the contour provided only a limited number of isolated attacks (Fig. 16c).

To investigate this different behaviors, local microstructural variations were investigated. In the core part, the Mo-, Nb- and Si-rich precipitates provided a blocky morphology. These phases were mainly located at the grain boundaries and secondly in correspondence of the oxidized areas and center of the grains (Fig. 17a). Their presence was also found on the inner surface of the elongated macro-defects (Fig. 17c). The relative volume fraction was 3.2 %. Instead, the secondary phase found in the contour part was characterized by an elongated morphology, clearly following the grain boundaries borders (Fig. 17b). Moreover, its presence was also detected on the inner surface of the elongated macro-defects (Fig. 17d). The relative volume fraction was 1.0 %. To further assess a possible variation in terms of phase composition between the core and contour, a comparative XRD analysis was conducted (Fig. 17e). Although, no significant difference was found between the two portions of the MEX-produced alloy 625 as a result of this test.

It is worth mentioning that the MEX-produced samples had a higher C content with respect to the all the other conditions investigated in this work (Table 1). Whether carbon pick-up occurred during the sintering phase, due to the decomposition of the residual binder, is still unclear. However, similar phenomena were reported by other authors. For instance, Horke et al. [63] reported that carbon enrichment occurs in the alloy 625 processed via metal injection molding (MIM) due to its pick-up from the atmosphere and/or the binder during the debinding and sintering phases. Additionally, Thompson et al. [32] declared that an increase in carbon content, causing carbides formation, occurred in MEX-produced alloy 718. It is evident that these phenomena are mainly linked to the thermal decomposition of the binder during the debinding and sintering steps. The shape, length and width of the open channels might determine how easily the decomposition byproducts escape and/or permeate the material. Therefore, it can be assumed that the different scanning strategies adopted influence the ability of the byproducts of the polymer decomposition to leave the specimens, thus influencing the local microstructure of the material. This seems to be confirmed by the increased C content in the secondary phases (Fig. 13b) and their frequent localization in correspondence of the edge of the defects (Fig. 11c, 17c).

In general, the precipitation of secondary phases might induce a degradation of the corrosion resistance in Ni alloys [74]. This effect is mostly due to the relative depletion of some elements from the matrix (γ), which results in an increase susceptibility to intergranular corrosion. For example, Mo depletion is a well-known cause for preferential corrosion [75]. Considering binder jetting, another AM technology relying on a polymeric binder, Mostafaei et al. [76] reported massive carbides formation, causing significant Mo, Nb and Cr depletion in large areas. It is also worth considering that the precipitates in the core appeared larger and more frequent than those in the contour, suggesting a more intense element depletion from the Ni matrix. Hence, the higher susceptibility to corrosion in the core portion of the material was probably due to a more significant depletion of protecting elements (Mo, Nb) from the surrounding grains. In general, the corrosion follows the microstructural features highlighted in the MEX-manufactured alloy 625. Furthermore, the material provided local morphological phase variations that were reflected by a different behavior of the core and contour portions during the susceptibility to intergranular corrosion test.

4. Conclusions

In this work, different AM technologies (PBF-LB, DED-LB, MEX) were considered to produce alloy 625 samples that were investigated in terms of defectology, microstructure, hardness and corrosion behavior. This paper focused on these aspects due to the lack of a material-based approach in the current literature. Furthermore, an initial assessment of the corrosion behavior was conducted due to its primary importance for the industrial fields of applications of the alloy 625. This work lays the foundation for more advanced corrosion analyses in future works. Great attention

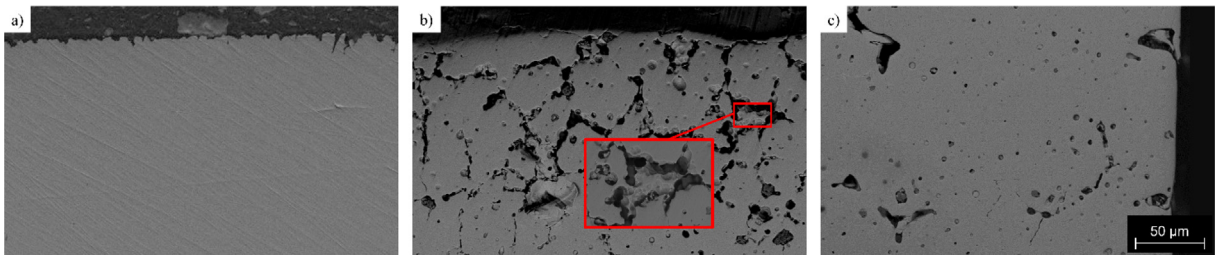

Fig. 16. Different response of the DED-LB- (a) and MEX-processed material during the susceptibility to intergranular corrosion test in the core (b) and contour (c) regions.

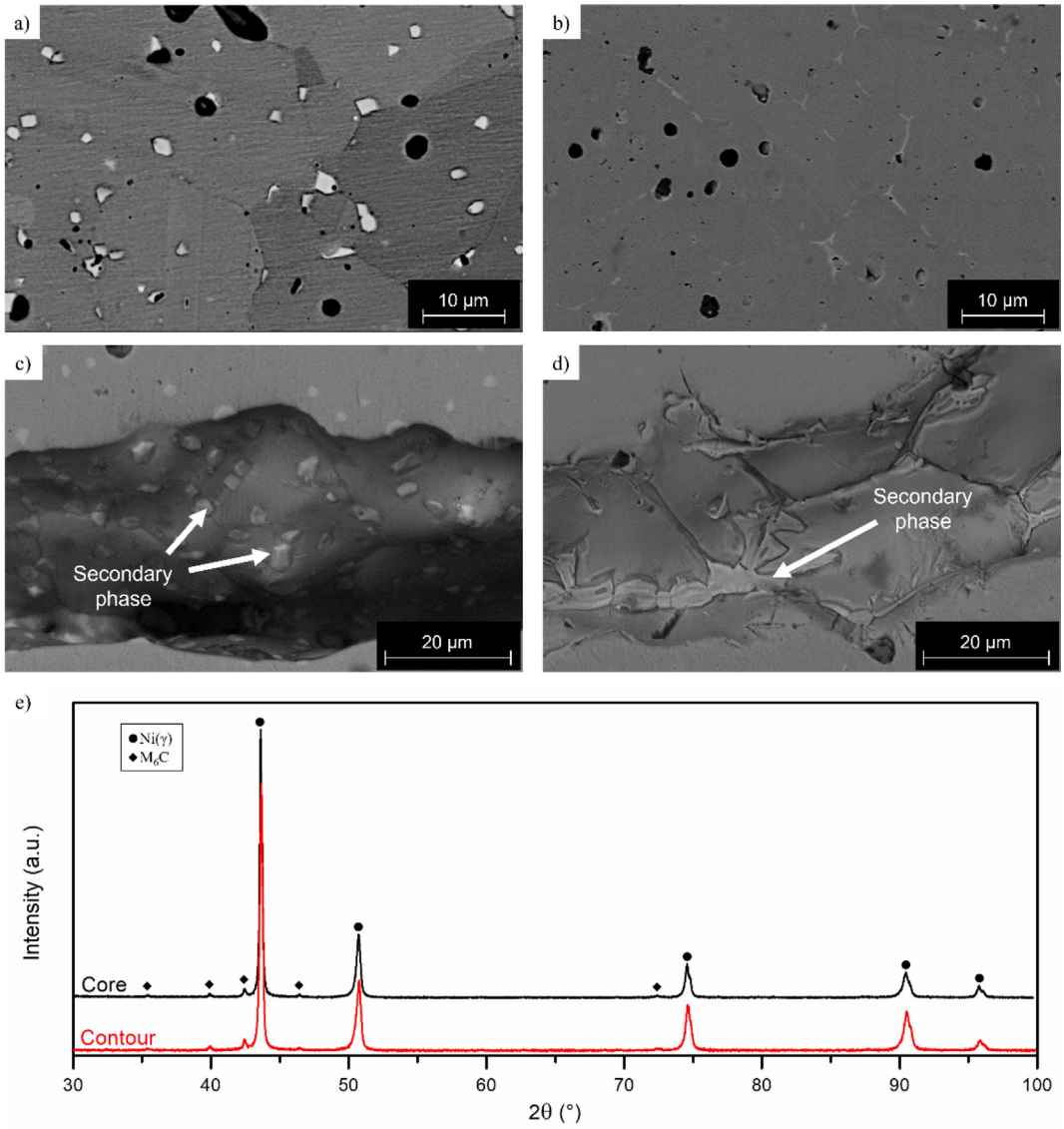

Fig. 17. Different microstructural features in the microstructure (a,b) and inside the elongated macro-defects (c,d) in the core and contour of the MEX-produced alloy 625, respectively. Comparison of the XRD patterns of the core and contour (e).

was dedicated to the MEX-processed material, given the current literature gap on the subject. The main results underlined in this work can be summarized as follows:

- The PBF-LB- and DED-LB-processed specimens provided very low porosity values. Conversely, the material processed via MEX was characterized by a significant amount of defects.
- In the MEX-built material were found small pores, both pre-existing in the feedstock material and generated during the debinding phase. Moreover, periodically distributed elongated macro-defects, result of the scanning strategy adopted, were also detected.
- A microCT analysis allowed to reconstruct the 3D shape of the macro-defects. These were significantly elongated and multiple stripes-long. In particular, long channels crossing the entire sample were found in the contour.
- Even if the microCT did not detect the smallest pores, accounting for the majority of the porosity, it provided crucial insight of the connectivity of the macro-defects and their spatial arrangement. The information gathered were used to develop an equation to better quantify the porosity from the data of the optical analysis, which might have led to an underestimation of this value.
- The PBF-LB- and DED-LB-built samples provided a microstructure coherent with the existing literature. The MEX-processed material was characterized by equiaxed γ grains with Mo-, Nb- and Si- rich second phases. These provided a blocky morphology in the core and an elongated shape in the contour.
- The highest hardness was provided by the samples manufactured via PBF-LB. The DED-LB-processed material had a lower value, due to the coarser dendritic microstructure. Instead, the MEX-built specimens were characterized by the lowest hardness, due to the complete disappearance of the dendritic structure.
- Whilst the PBF-LB and DED-LB-processed materials provided negligible intergranular corrosion, the MEX-built specimens resulted in significant localized attacks in the core region, proving that the response during the test was strictly determined by the microstructural features detected.

Data availability

Data will be made available on request.

Declaration of Competing Interest

The authors declare that they have no known competing financial interests or personal relationships that could have appeared to influence the work reported in this paper.

Acknowledgements

This research work has been funded by Regione Lombardia (Italy), regional law n° 9/2020, resolution n° 3776/2020.

References

[1] M. Karmuhilan, S. Kumanan, A Review on Additive Manufacturing Processes of Inconel 625, J. Mater. Eng. Perform. 1–10 (2021).
[2] V. Shankar, K.B.S. Rao, S.L. Mannan, Microstructure and mechanical properties of Inconel 625 superalloy, J. Nucl. Mater. 288 (2001) 222–232.
[3] Y. Tian, B. Ouyang, A. Gontcharov, R. Gauvin, P. Lowden, M. Brochu, Microstructure evolution of Inconel 625 with 0.4 wt% boron modification during gas tungsten arc deposition, J Alloys Compd. 694 (2017) 429–438.
[4] M. Cabrini, S. Lorenzi, C. Testa, F. Carugo, T. Pastore, D. Manfredi, S. Biamino, G. Marchese, S. Parizia, F. Scenini, Stress Corrosion Cracking of Additively Manufactured Alloy 625, Materials. 14 (2021) 6115.
[5] G.D. Smith, N.C. Eisinger, The effect of niobium on the corrosion resistance of nickel-base alloys, in: Proc Int Symp Niobium High Temp Appl, 2004: pp. 23–34.
[6] E.L. Hibner, CORROSION/86, paper no. 181, NACE International, Houston, TX, 1986.
[7] C.P. Paul, P. Ganesh, S.K. Mishra, P. Bhargava, J.A. Negi, A.K. Nath, Investigating laser rapid manufacturing for Inconel-625 components, Opt Laser Technol. 39 (2007) 800–805.
[8] Y. Gao, Y. Ding, J. Chen, J. Xu, Y. Ma, X. Wang, Effect of twin boundaries on the microstructure and mechanical properties of Inconel 625 alloy, Mater. Sci. Eng. A 767 (2019) 138361.
[9] Y.L. Hu, X. Lin, X.B. Yu, J.J. Xu, M. Lei, W.D. Huang, Effect of Ti addition on cracking and microhardness of Inconel 625 during the laser solid forming processing, J Alloys Compd. 711 (2017) 267–277.
[10] Y. AbouelNour, N. Gupta, In-situ monitoring of sub-surface and internal defects in additive manufacturing: A review, Mater Des. 222 (2022), https://doi.org/10.1016/j.matdes.2022.111063 111063.
[11] W.E. Frazier, Metal additive manufacturing: A review, J. Mater. Eng. Perform. 23 (2014) 1917–1928, https://doi.org/10.1007/s11665-014-0958-z.
[12] G. Sander, J. Tan, P. Balan, O. Gharbi, D.R. Feenstra, L. Singer, S. Thomas, R.G. Kelly, J.R. Scully, N. Birbilis, Corrosion of additively manufactured alloys: a review, Corrosion 74 (2018) 1318–1350.
[13] S.A.M. Tofail, E.P. Koumoulos, A. Bandyopadhyay, S. Bose, L. O'Donoghue, C. Charitidis, Additive manufacturing: scientific and technological challenges, market uptake and opportunities, Mater. Today 21 (2018) 22–37.
[14] T. Pichler, J.H. Schleifenbaum, Examination of the LPBF Process by Means of Thermal Imaging for the Development of a Geometric-specific Process Control, In: 2019 International Solid Freeform Fabrication Symposium, University of Texas at Austin, 2019.
[15] A. Khorasani, I. Gibson, J.K. Veetil, A.H. Ghasemi, A review of technological improvements in laser-based powder bed fusion of metal printers, Int. J. Adv. Manuf. Technol. 108 (2020) 191–209.
[16] S. Cao, Y. Zou, C.V.S. Lim, X. Wu, Review of laser powder bed fusion (LPBF) fabricated Ti-6Al-4V: process, post-process treatment, microstructure, and property, Light Adv. Manuf. 2 (2021) 313–332.
[17] L. Dowling, J. Kennedy, S. O'Shaughnessy, D. Trimble, A review of critical repeatability and reproducibility issues in powder bed fusion, Mater. Des. 186 (2020), https://doi.org/10.1016/j.matdes.2019.108346 108346.
[18] M. Cabrini, A. Carrozza, S. Lorenzi, T. Pastore, C. Testa, D. Manfredi, P. Fino, F. Scenini, Influence of surface finishing and heat treatments on the corrosion resistance of LPBF-produced Ti-6Al-4V alloy for biomedical applications, J. Mater. Process Technol. 308 (2022) 117730.
[19] A.N. Jinoop, C.P. Paul, K.S. Bindra, Laser-assisted directed energy deposition of nickel super alloys: a review, Proceedings of the Institution of Mechanical Engineers, Part L: Journal of Materials: Design and Applications. 233 (2019) 2376–2400.
[20] A. Dass, A. Moridi, State of the art in directed energy deposition: From additive manufacturing to materials design, Coatings 9 (2019) 418.
[21] A. Carrozza, F. Mazzucato, A. Aversa, M. Lombardi, F. Bondioli, S. Biamino, A. Valente, P. Fino, Single Scans of Ti-6Al-4V by Directed Energy Deposition: A Cost and Time Effective Methodology to Assess the Proper Process Window, Met. Mater. Int. 27 (2021), https://doi.org/10.1007/s12540-020-00930-3.
[22] P. Singh, V.K. Balla, A. Tofangchi, S.v. Atre, K.H. Kate, Printability studies of Ti-6Al-4V by metal fused filament fabrication (MF3), Int. J. Refract. Metals Hard Mater. 91 (2020) 105249.
[23] Y. Thompson, J. Gonzalez-Gutierrez, C. Kukla, P. Felfer, Fused filament fabrication, debinding and sintering as a low cost additive manufacturing method of 316L stainless steel, Addit Manuf. 30 (2019) 100861.
[24] V.B. Nidagundi, R. Keshavamurthy, C.P.S. Prakash, Studies on parametric optimization for fused deposition modelling process, Mater. Today Proc. 2 (2015) 1691–1699.
[25] H. Ramazani, A. Kami, Metal FDM, a new extrusion-based additive manufacturing technology for manufacturing of metallic parts: a review, Progress in Additive Manufacturing. (2022) 1–18.
[26] B. Liu, Y. Wang, Z. Lin, T. Zhang, Creating metal parts by fused deposition modeling and sintering, Mater. Lett. 263 (2020) 127252.
[27] M. Carminati, M. Quarto, G. D'Urso, C. Giardini, G. Maccarini, Mechanical characterization of AISI 316L samples printed using material extrusion, Appl. Sci. 12 (2022) 1433.
[28] J. Gonzalez-Gutierrez, F. Arbeiter, T. Schlauf, C. Kukla, C. Holzer, Tensile properties of sintered 17–4PH stainless steel fabricated by material extrusion additive manufacturing, Mater. Lett. 248 (2019) 165–168.
[29] D. Godec, S. Cano, C. Holzer, J. Gonzalez-Gutierrez, Optimization of the 3D printing parameters for tensile properties of specimens produced by fused filament fabrication of 17–4PH stainless steel, Materials. 13 (2020) 774.
[30] L. Ren, X. Zhou, Z. Song, C. Zhao, Q. Liu, J. Xue, X. Li, Process parameter optimization of extrusion-based 3D metal printing utilizing PW–LDPE–SA binder system, Materials. 10 (2017) 305.
[31] Z. Lu, O.I. Ayeni, X. Yang, H.-Y. Park, Y.-G. Jung, J. Zhang, Microstructure and phase analysis of 3d-printed components using bronze metal filament, J. Mater. Eng. Perform. 29 (2020) 1650–1656.
[32] Y. Thompson, K. Zissel, A. Förner, J. Gonzalez-Gutierrez, C. Kukla, S. Neumeier, P. Felfer, Metal fused filament fabrication of the nickel-base superalloy IN 718, J. Mater. Sci. 57 (2022) 9541–9555.
[33] A. Riaz, P. Töllner, A. Ahrend, A. Springer, B. Milkereit, H. Seitz, Optimization of composite extrusion modeling process parameters for 3D printing of low-alloy steel AISI 8740 using metal injection moulding feedstock, Mater. Des. 219 (2022), https://doi.org/10.1016/j.matdes.2022.110814 110814.
[34] J. Costa, E. Sequeiros, M.T. Vieira, M. Vieira, Additive manufacturing: Material extrusion of metallic parts, U. Porto, J. Eng. 7 (2021) 53–69.
[35] D. Thomas, A. Gleadall, Advanced metal transfer additive manufacturing of high temperature turbine blades, Int. J. Adv. Manuf. Technol. 120 (2022) 6325–6335.
[36] P. Ganesan, C.M. Renteria, J.R. Crum, Versatile corrosion resistance of Inconel alloy 625 in various aqueous and chemical processing environments, Superalloys. 718 (1991) 663–680.
[37] G. Marchese, E. Bassini, S. Parizia, D. Manfredi, D. Ugues, M. Lombardi, P. Fino, S. Biamino, Role of the chemical homogenization on the microstructural and mechanical evolution of prolonged heat-treated laser powder bed fused Inconel 625, Mater. Sci. Eng. A 796 (2020), https://doi.org/10.1016/j.msea.2020.140007 140007.
[38] Y.L. Hu, Y.L. Li, S.Y. Zhang, X. Lin, Z.H. Wang, W.D. Huang, Effect of solution temperature on static recrystallization and ductility of Inconel 625 superalloy fabricated by directed energy deposition, Mater. Sci. Eng. A 772 (2020) 138711.
[39] T. Chen, Y. Chen, J. Jiao, Y. Wang, L. Qian, Z. Guo, Z. Ma, C. Han, T. Shi, Comparison of the effectiveness and safety of topical versus intravenous tranexamic acid in primary total knee arthroplasty: a meta-analysis of randomized controlled trials, J. Orthop. Surg. Res. 12 (2017) 1–11.
[40] M. Cabrini, S. Lorenzi, C. Testa, T. Pastore, F. Brevi, S. Biamino, P. Fino, D. Manfredi, G. Marchese, F. Calignano, F. Scenini, Evaluation of Corrosion Resistance of Alloy 625 Obtained by Laser Powder Bed Fusion, J. Electrochem. Soc. 166 (2019) C3399–C3408, https://doi.org/10.1149/2.0471911jes.
[41] M. Santini, S. Fest-Santini, P. Foltyn, On the local mass transfer rates around arbitrary shaped particles calculated by X-ray computed microtomography: prospective for a novel experimental technique, Int. Commun. Heat Mass Transfer 79 (2016) 135–139.
[42] B.D. Cullity, Elements of X-ray Diffraction, Addison-Wesley Publishing, 1956.
[43] A. Carrozza, G. Marchese, A. Saboori, E. Bassini, A. Aversa, F. Bondioli, D. Ugues, S. Biamino, P. Fino, Effect of Aging and Cooling Path on the Super β-Transus Heat-Treated Ti-6Al-4V Alloy Produced via Electron Beam Melting (EBM), Materials. 15 (2022) 4067.
[44] H. Wong, K. Dawson, G.A. Ravi, L. Howlett, R.O. Jones, C.J. Sutcliffe, Multi-laser powder bed fusion benchmarking—Initial trials with Inconel 625, Int. J. Adv. Manuf. Technol. 105 (2019) 2891–2906.
[45] J.-R. Poulin, A. Kreitcberg, P. Terriault, V. Brailovski, Long fatigue crack propagation behavior of laser powder bed-fused inconel 625 with intentionally-seeded porosity, Int. J. Fatigue. 127 (2019) 144–156.
[46] A. Evangeline, P. Sathiya, Structure–property relationships of Inconel 625 cladding on AISI 316L substrate produced by hot wire (HW) TIG metal deposition technique, Mater. Res. Express. 6 (2019) 106539.
[47] J.-R. Poulin, A. Kreitcberg, V. Brailovski, Effect of hot isostatic pressing of laser powder bed fused Inconel 625 with purposely induced defects on the residual porosity and fatigue crack propagation behavior, Addit. Manuf. 47 (2021) 102324.
[48] R. Fu, S. Tang, J. Lu, Y. Cui, Z. Li, H. Zhang, T. Xu, Z. Chen, C. Liu, Hot-wire arc additive manufacturing of aluminum alloy with reduced porosity and high deposition rate, Mater. Des. 199 (2021) 109370.

[49] M. Suard, G. Martin, P. Lhuissier, R. Dendievel, F. Vignat, J.-J. Blandin, F. Villeneuve, Mechanical equivalent diameter of single struts for the stiffness prediction of lattice structures produced by Electron Beam Melting, Addit. Manuf. 8 (2015) 124–131, https://doi.org/10.1016/j.addma.2015.10.002.
[50] A. du Plessis, I. Yadroitsava, I. Yadroitsev, Effects of defects on mechanical properties in metal additive manufacturing: A review focusing on X-ray tomography insights, Mater. Des. 187 (2020), https://doi.org/10.1016/j.matdes.2019.108385 108385.
[51] N. Otsu, A threshold selection method from gray-level histograms, IEEE Trans. Syst. Man Cybern. 9 (1979) 62–66.
[52] Z. Tian, C. Zhang, D. Wang, W. Liu, X. Fang, D. Wellmann, Y. Zhao, Y. Tian, A review on laser powder bed fusion of inconel 625 nickel-based alloy, Appl. Sci. 10 (2019) 81.
[53] M. Rombouts, G. Maes, M. Mertens, W. Hendrix, Laser metal deposition of Inconel 625: Microstructure and mechanical properties, J. Laser Appl. 24 (2012) 052007.
[54] Y. Wang, X. Chen, Q. Shen, C. Su, Y. Zhang, S. Jayalakshmi, R.A. Singh, Effect of magnetic Field on the microstructure and mechanical properties of inconel 625 superalloy fabricated by wire arc additive manufacturing, J. Manuf. Process. 64 (2021) 10–19.
[55] Y. Gao, Y. Ding, Y. Ma, J. Chen, X. Wang, J. Xu, Evolution of annealing twins in Inconel 625 alloy during tensile loading, Mater. Sci. Eng. A 831 (2022) 142188.
[56] G. Marchese, S. Parizia, M. Rashidi, A. Saboori, D. Manfredi, D. Ugues, M. Lombardi, E. Hryha, S. Biamino, The role of texturing and microstructure evolution on the tensile behavior of heat-treated Inconel 625 produced via laser powder bed fusion, Mater. Sci. Eng. A 769 (2020) 138500.
[57] G. de Leon Nope, G. Wang, J.M. Alvarado-Orozco, B. Gleeson, Role of Elemental Segregation on the Oxidation Behavior of Additively Manufactured Alloy 625, JOM 74 (2022) 1698–1706.
[58] G. Marchese, M. Lorusso, S. Parizia, E. Bassini, J.-W. Lee, F. Calignano, D. Manfredi, M. Terner, H.-U. Hong, D. Ugues, Influence of heat treatments on microstructure evolution and mechanical properties of Inconel 625 processed by laser powder bed fusion, Mater. Sci. Eng. A 729 (2018) 64–75.
[59] T.E. Abioye, P.K. Farayibi, A.T. Clare, A comparative study of Inconel 625 laser cladding by wire and powder feedstock, Mater. Manuf. Process. 32 (2017) 1653–1659.
[60] W. Yangfan, C. Xizhang, S. Chuanchu, Microstructure and mechanical properties of Inconel 625 fabricated by wire-arc additive manufacturing, Surf. Coat. Technol. 374 (2019) 116–123.
[61] Y.L. Hu, X. Lin, Y.L. Li, S.Y. Zhang, X.H. Gao, F.G. Liu, X. Li, W.D. Huang, Plastic deformation behavior and dynamic recrystallization of Inconel 625 superalloy fabricated by directed energy deposition, Mater. Des. 186 (2020), https://doi.org/10.1016/j.matdes.2019.108359 108359.
[62] J. Huebner, D. Kata, J. Kusiński, P. Rutkowski, J. Lis, Microstructure of laser cladded carbide reinforced Inconel 625 alloy for turbine blade application, Ceram. Int. 43 (2017) 8677–8684.
[63] K. Horke, A. Meyer, R.F. Singer, Metal injection molding (MIM) of nickel-base superalloys, in: Handbook of Metal Injection Molding, Elsevier, 2019: pp. 575–608.
[64] F. Yang, L. Dong, X. Hu, X. Zhou, Z. Xie, F. Fang, Effect of solution treatment temperature upon the microstructure and mechanical properties of hot rolled Inconel 625 alloy, J. Mater. Sci. 55 (2020) 5613–5626.
[65] X.W. Li, L. Wang, J.S. Dong, L.H. Lou, Effect of solidification condition and carbon content on the morphology of MC carbide in directionally solidified nickel-base superalloys, J. Mater. Sci. Technol. 30 (2014) 1296–1300.
[66] G. Marchese, E. Bassini, A. Aversa, M. Lombardi, D. Ugues, P. Fino, S. Biamino, Microstructural evolution of post-processed Hastelloy X alloy fabricated by laser powder bed fusion, Materials. 12 (2019) 486.
[67] Z. Xu, L. Jiang, J. Dong, Z. Li, X. Zhou, The effect of silicon on precipitation and decomposition behaviors of M6C carbide in a Ni–Mo–Cr superalloy, J Alloys Compd. 620 (2015) 197–203.
[68] M. Qunshuang, L. Yajiang, W. Juan, L. Kun, Homogenization of carbides in Ni60/WC composite coatings made by fiber laser remelting, Mater. Manuf. Process. 30 (2015) 1417–1424.
[69] J.F. Radavich, A. Fort, Effects of long-time exposure in alloy 625 at, Superalloys. 718 (1994) 635–647.
[70] Q. Guo, Y. Li, J. Qian, H. Yu, C. Chen, Study of the pitting corrosion at welding joints of Inconel 625 alloy under high temperature and high H2S/CO2 partial pressure, Int. J. Electrochem. Sci. 12 (2017) 8929–8943.
[71] L. Ferrer, B. Pieraggi, J.F. Uginet, Thermomechanical Processing of Alloy 625, Superalloys. 718 (1991) 625–706.
[72] M.J. Cieslak, T.J. Headley, A.D. Romig, T. Kollie, A melting and solidification study of alloy 625, Metall. Trans. A 19 (1988) 2319–2331.
[73] M. Cabrini, S. Lorenzi, C. Testa, F. Brevi, S. Biamino, P. Fino, D. Manfredi, G. Marchese, F. Calignano, T. Pastore, Microstructure and selective corrosion of alloy 625 obtained by means of laser powder bed fusion, Materials. 12 (2019) 1–11, https://doi.org/10.3390/ma12111742.
[74] G.V.B. Lemos, A.B. Farina, H. Piaggio, L. Bergmann, J.Z. Ferreira, J.F. dos Santos, G. vander Voort, A. Reguly, Mitigating the susceptibility to intergranular corrosion of alloy 625 by friction-stir welding, Sci. Rep. 12 (2022) 1–9.
[75] L. Xu, J. Zhang, Y. Han, L. Zhao, H. Jing, Insights into the intergranular corrosion of overlay welded joints of X65-Inconel 625 clad pipe and its relationship to damage penetration, Corros. Sci. 160 (2019) 108169.
[76] A. Mostafaei, J. Toman, E.L. Stevens, E.T. Hughes, Y.L. Krimer, M. Chmielus, Microstructural evolution and mechanical properties of differently heat-treated binder jet printed samples from gas-and water-atomized alloy 625 powders, Acta Mater. 124 (2017) 280–289.